APPENDIX 1: INSTRUMENTATION AND CHARACTERIZATION TECHNIQUES

Instrumentations that were involved for characterization of the synthesized nanoparticles and the SERS substrate samples have been covered here. The principle of operation of other assays such as enzyme-linked immunosorbent assay (ELISA) and polymerase chain reaction (PCR) which have been used in the research work have been narrated.

Transmission electron microscopy (TEM) instrumentation

Transmission electron microscopy (TEM) is a type of electron microscopy which is employed to study the morphology of the nanostructured material [1]. A schematic illustration of TEM instrumentation is depicted in the figure 7.1. In this instrument, high energy (100 - 500 KeV) electrons are generated from the electron gun and passes through the condenser lens which controls the convergence angle and the diameter of the electron beam. This beam then incident on the sample and transmitted through the same. The transmitted beam is then passes through objective lens, intermediate lens and projector lens. The intermediate lens is used to change between transmitted mode and image mode of TEM instrument. The projector lens projects the magnified image, which carries the morphological information of the sample, on the fluorescent screen.

In the present thesis, a TEM instrument (Model number: TECNAI G2 20 S-TWIN) from FEI COMPANY, USA equiped with selected area electron diffraction (SAED) facility is used to study the morphologies of the synthesized metal nanoparticles. The nanoparticles were drop-casted on carbon coated copper mesh TEM grid and dried for overnight at room temperature before collecting the TEM images.

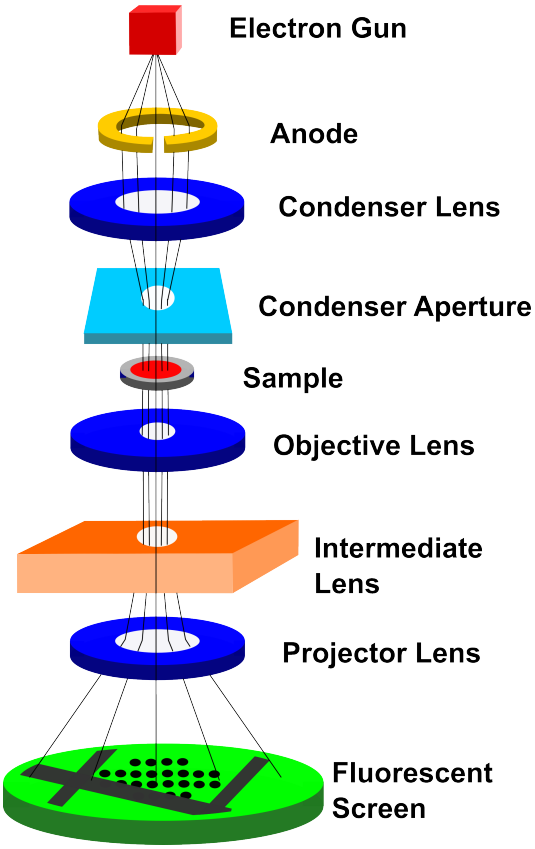

Figure 7.1: Schematic representation of TEM instrumentation.

Scanning electron microscopy (SEM) and field emission scanning electron microscopy (FESEM) instrumentation

SEM and FESEM are a type of elcetron microscopes which are used to characterize the morphology of the nanostructered surfaces [2]. Both systems follow the same principle, the only distinction is in the electron generation. A schematic illustration of SEM instrumentation is shown in the figure 7.2. A sample is inserted inside the instrument and kept in a vacuum condition. High energetic electrons (few eV to 100 KeV) are generated from the electron source placed at the top of the column. A set of condenser lenses are used to form a narrow beam of electrons, and an objective lens to focus the beam on the sample to illuminate it. After interacting with the surface of the sample, the electrons generate secondary electrons, back scattered electrons and characteristic X-rays which are collected by different detectors.

During the present thesis work, a SEM instrument (Model number: JSM 6390LV) and FESEM instrument (Model number: JSM7200F) from JEOL, Japan have been utilised for studying the morphology of the fabricated SERS substrates. SERS substrates to be characterized are attached to the metallic sample holder with a double

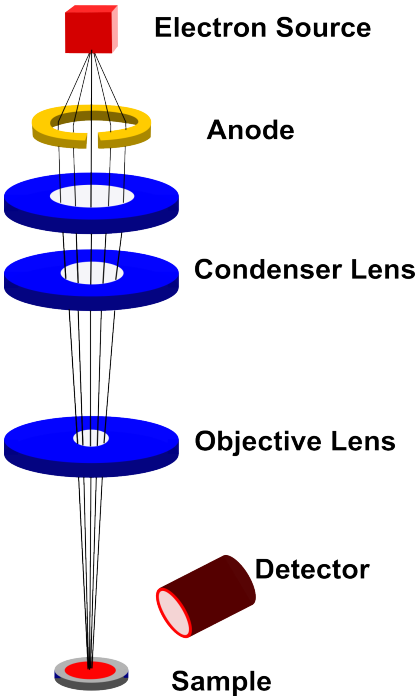

Figure 7.2: Schematic representation of SEM instrumentation.

sided conducting carbon tape. A thin film of platinum is sputtered over the sample surface to avoid the surface charging effect before the scanning. SEM and FESEM micrographs are collected from several positions on the sample at different magnification values.

UV-Visible spectroscopy instrumentation

UV-Visible spectroscopy is another popular instrument for characterization of metal nanoparticles. It is based on the principle of light absorption by a material sample [3]. Design of a typical UV-Visible spectrometer is shown in the figure 7.3. This instrument is equiped with ultraviolet, visible and NIR light sources. Monochromator is used to select a narrow band of light to interact with the sample and the reference. A portion of the incident light is absorbed by the medium, and the transmitted light is recorded as a function of wavelength using appropriate detectors. In the present work, UV-Visible spectrometer is used to study the plasmonic properties of the synthesized metal nanoparticles.

Enzyme-linked immunosorbent assay (ELISA)

The catalytic properties of enzymes have been utilized by enzyme immunoassays (EIAs) for detecting and analyzing immunological reactions. A heterogeneous EIA technique named enzyme-linked immunosorbent assay (ELISA) has been extensively used in clini-

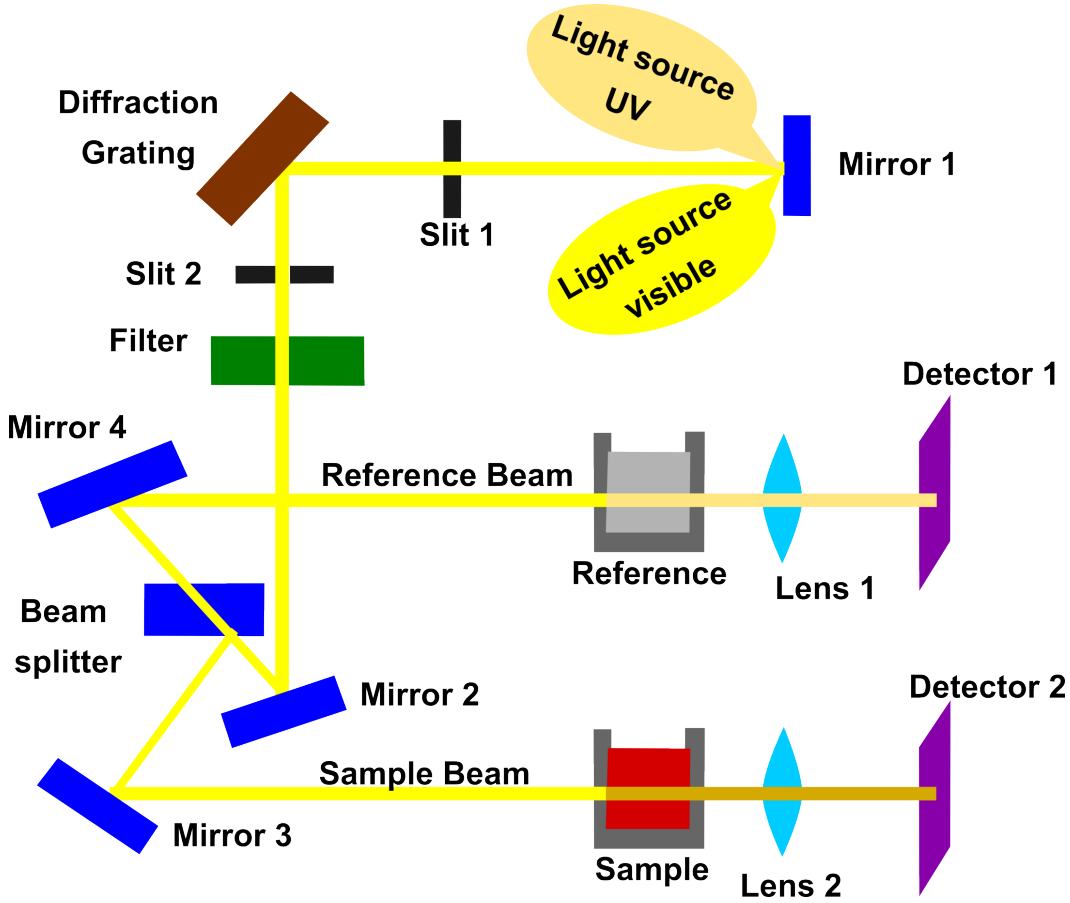

Figure 7.3: Schematic representation of UV-Visible spectrometer instrumentation.

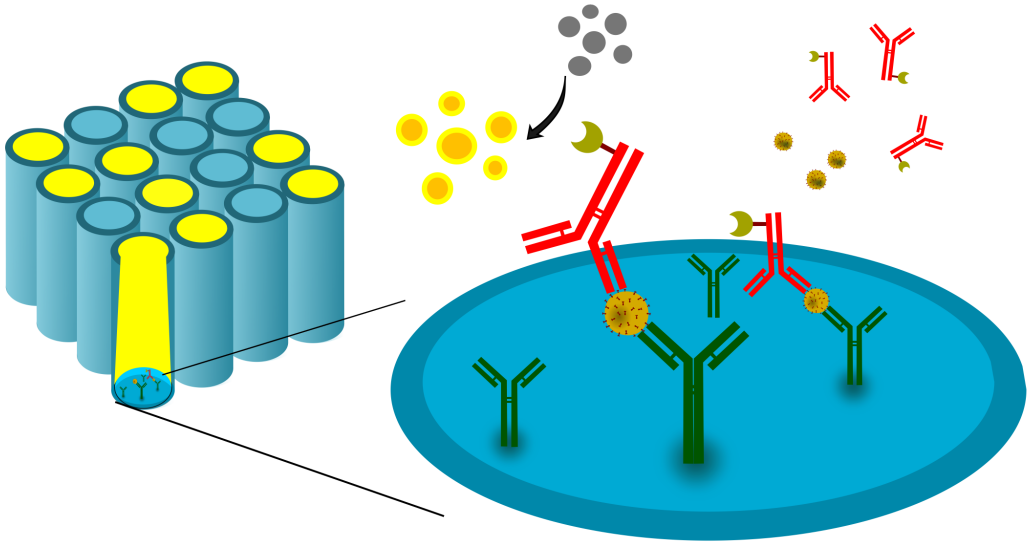

Figure 7.4: Schematic representation of sandwich ELISA.

cal analysis. Here, one of the reaction component is covalently bound or nonspecifically adsorbed to the surface of a solid phase, such as a plastic bead, magnetic particle, or microtiter well [4, 5].

Polymerase chain reaction (PCR)

Polymerase chain reaction (PCR) technique allows the amplification of a specific DNA fragment from a complex pool of DNA [6, 7]. This technique is very sensitive as only small amount of DNA is required to produce sufficient copies of DNA using conventional laboratory steps. DNA polymerase, primers, nucleotides, and template DNA are needed for every PCR test. In the DNA, there are the four nucleobases – adenine, thymine, cytosine, and guanine. The DNA polymerase is the enzyme that connects individual nucleotides together to generate the PCR product. Primers are short DNA fragments which has a defined sequence complementary to the target DNA.

Bibliography

[1] Williams, D. B., Carter, C. B., Williams, D. B., and Carter, C. B. *The transmission electron microscope*. Springer, 1996.

[2] Goodhew, P. J. and Humphreys, J. *Electron microscopy and analysis*. CRC press, 2000.

[3] Perkampus, H.-H. *UV-VIS Spectroscopy and its Applications*. Springer Science & Business Media, 2013.

[4] Aydin, S. A short history, principles, and types of elisa, and our laboratory experience with peptide/protein analyses using elisa. *Peptides*, 72:4–15, 2015.

[5] Alhajj, M., Zubair, M., and Farhana, A. Enzyme linked immunosorbent assay. *StatPearls*, 2023.

[6] Mullis, K. B. The unusual origin of the polymerase chain reaction. *Scientific American*, 262(4):56–65, 1990.

[7] Garibyan, L. and Avashia, N. Research techniques made simple: polymerase chain reaction (pcr). *The Journal of investigative dermatology*, 133(3):e6, 2013.

APPENDIX 2: ELECTROMAGNETIC SIMULATION USING COMSOL MULTIPHYSICS SOFTWARE

In the SERS technique, the analyte molecules adsorbed on, or near the hot-spot regions of metal nanostructures such as gold and silver, and thus provide a highly scattered Raman signal. As discussed in the section 1.3.1 of Chapter 1, this signal enhancement is mostly due to the electromagnetic enhancement mechanism. The incident laser light interacts with the metal nanoparticles and generates strong LSPR field in the vicinity of the nanoparticles. The LSPR field magnitude of the metal nanoparticle system in SERS substrate depends on the size, shape, material, interparticle spacing of nanoparticles, the incident laser wavelength, and the ambience of analyte. The nanoparticles are synthesized by wet chemical method, or more complex and time consuming lithographic techniques. Therefore, it is prefarable to study and optimize the LSPR field required for a given application first using a simulation tool which could minimize time and fabrication cost to the lowest possible, or one can have an idea about the magnitude of the coupled electromagnetic field in the hot-spot regions of the proposed SERS platform.

Model definition

Using FEM, Maxwell's electromagnetic equation in three dimension for a new structures of any arbitrary shapes can be solved. FEM-based COMSOL Multiphysics software (Wave Optics Module) have been used to calculate the scattered electric field (E_{sc}) and the electromagnetic enhancement [1] using the following equation:

$$\bigtriangledown \times \left[\frac{1}{\mu_r}\left(\bigtriangledown \times E_{sc}\right)\right] - K_0^2\left[\left(\varepsilon_r - \frac{j\sigma}{\omega\varepsilon_0}\right)\right] E_{sc} = 0. \tag{7.1}$$

Here, μ_r and ε_r represents the relative permeability and permittivity of the medium, respectively. K_0 is the wavenumber in free space.

User interface of the COMSOL software has been depicted in the figure 7.5. Electromagnetic Waves, Frequency Domain interface of this software has been utilized in solving the scattered field which is a perturbation due a local scatterer to the total field [2]. The incident electromagnetic wave has been introduced as background electric field

which represents the solution of the wave equation in absence of the scatterer in the model. The expression of background field in the presense of a nanoparticle scatterer when placed on a substrate is the superposition of incident and reflected wave in the free space domain, and a transmitted wave in the substrate. In the two port condition, one port has been considered for the incident wave to get specular reflection, while transmitted plane waves have been absorbed by the other port. Floquet periodic conditions have been considered in the side boundaries of the model. A perfectly matched layer (PML) has been considered surrounding the whole domain which absorbs the scattered field and avoids any internal reflections that could add to the resultant electric field [3]. It is generally sufficient to place the PML half a wavelength distant from the scatterer to avoid it being in the scatterer's reactive near-field.

The scattering cross-section (σ_{sc}) is defined as:

$$\sigma_{sc} = \frac{1}{I_0} \iint (\mathbf{n} \cdot \mathbf{S}_{sc}) dS. \tag{7.2}$$

Here, I_0 is the intensity of the incident light, S_{sc} is the scattered intensity (Poynting vector), and $\mathbf{n}$ is the normal vector pointing outwards from the nanoparticle.

The absorption cross section (σ_{abs}) is measured as:

$$\sigma_{abs} = \frac{1}{I_0} \iiint Q dV. \tag{7.3}$$

Here, Q represents the power loss density in the nanoparticle, and the integral is taken over its volume.

The extinction cross section (σ_{ext}) can be expressed as:

$$\sigma_{ext} = \sigma_{sc} + \sigma_{abs}. \tag{7.4}$$

The simulations have been performed in the frequency range 350 nm to 800 nm, where the gold and silver have negative complex-valued permittivity. The refractive index of the materials have been selected from the Optical Materials Database in the softwate [4]. The electromagnetic enhancement factors (EFs) for different simulation models have been evaluated by fourth power of the ratio of near-electric field to the incident electric field [1].

Results and discussions

This simulation work demonstrates the effect of the parameters determining the localized electric field distribution and EF for a nanoparticle system. At first, scattered electric field for single AgNP and AuNP of diameter from 20 nm to 100 nm have been calculated. Figure 7.6(a) and 7.6(b) represent the scattered electric field and EF for 50

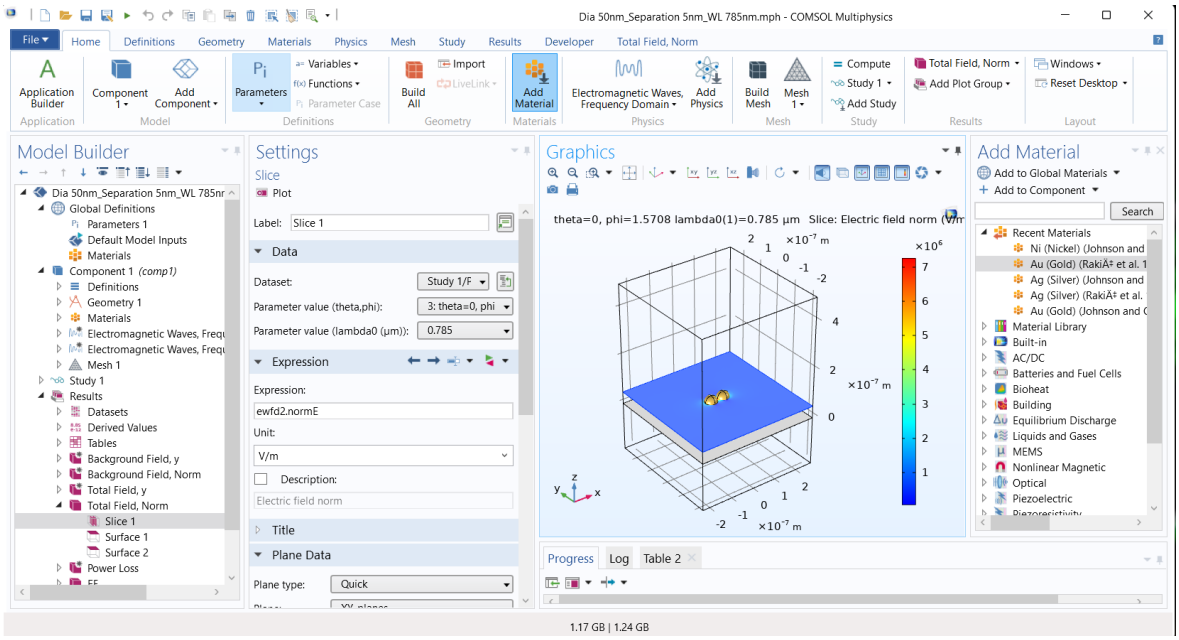

Figure 7.5: COMSOL Multiphysics simulation software interface.

nm AgNP for the incident laser wavelength 400 nm. Next, the the same nanoparticle has been excited with other higher wavelengths up to 800 nm, and the scattered electric field and EF are plotted in the figure 7.6(f). Similarly, AgNPs of different size have been excited with the laser wavelength from 350 nm to 800 nm, and the magnitude of coupled electric field have been calculated. The same steps are followed for a silver nanorod (AgNR) (length 100 nm, diameter 50 nm) and another AgNR (length 200 nm, diameter 50 nm), and excited with the laser of wavelength from 350 nm to 800 nm. The scattared electric field for the AgNR (length 100 nm, diameter 50 nm) excited with 500 nm wavelength is represented in the figure 7.6(c). Figure 7.6(d) and 7.6(e) represent the electic field for AgNR (length 200 nm, diameter 50 nm) excited with wavelengths 785 nm (d) and 1064 nm (e), respectively. Figure 7.6(g) and 7.6(h) represent the plot of electric field and EF for AgNR (length 100 nm, diameter 50 nm) and AgNR (length 200 nm, diameter 50 nm) at different incident laser wavelengths. From the figure 7.6(f), 7.6(g) and 7.6(h), it can be found that the field intensity shifts with the variation of the size and shape of nanoparticles, and wavelength of the incident laser.

Three arrangents, a single nanoparticle, a dimer, and a trimer of AuNPs of diameter 50 nm and interparticle gap 5 nm have been considered in air medium. In the figure 7.7, polar angle of incidence, ϕ of the plane polarized light is varied from $\phi = 0$ (a,d,g) to $\phi = \pi/4$ (b,e,h) and $\phi = \pi/2$ (c,f,i), keeping the azimuthal angle of incidence, θ fixed at $\theta = 0$. It can be found that with the change of polarization, the local electric field distibution changes. However, the localized electric field amplitude remains same for all three cases. In case of AuNP dimer, the indivisual electric field of the nanoparticles couples and generates strong electric field or hot-spot region for $\phi = \pi/4$ and $\phi =$

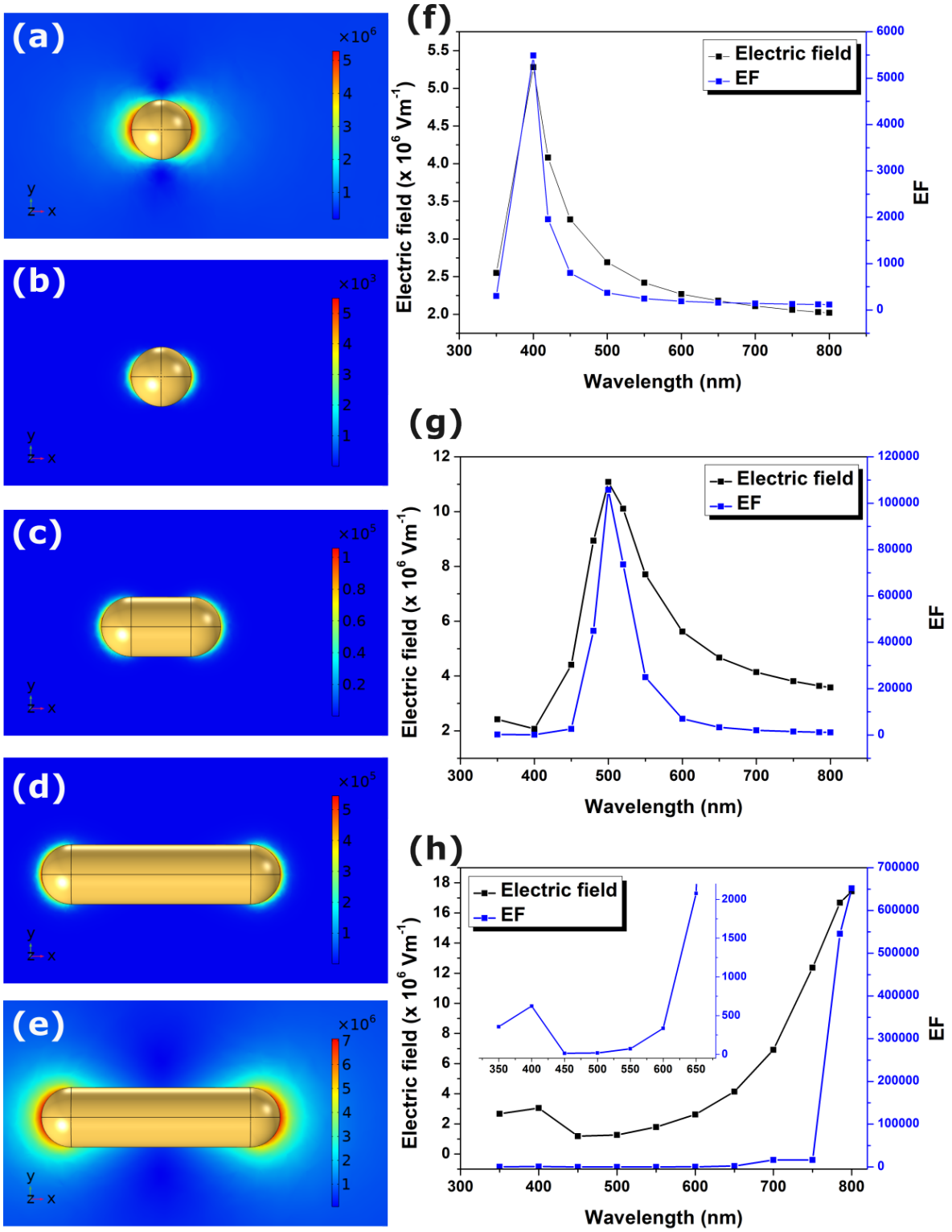

Figure 7.6: Scattered electric field (a) and EF (b) for a single AgNPs after exitation with a 400 nm light. Electric field for a AgNR (length 100 nm, diameter 50 nm) for 500 nm wavelength (c), AgNR (length 200 nm, diameter 50 nm) for wavelengths 785 nm (d) and 1064 nm (e). Plot of electric field and EF for (f) single AgNP (diameter 50 nm), (g) AgNR (length 100 nm, diameter 50 nm) and (h) AgNR (length 200 nm, diameter 50 nm) at different incident laser wavelengths.

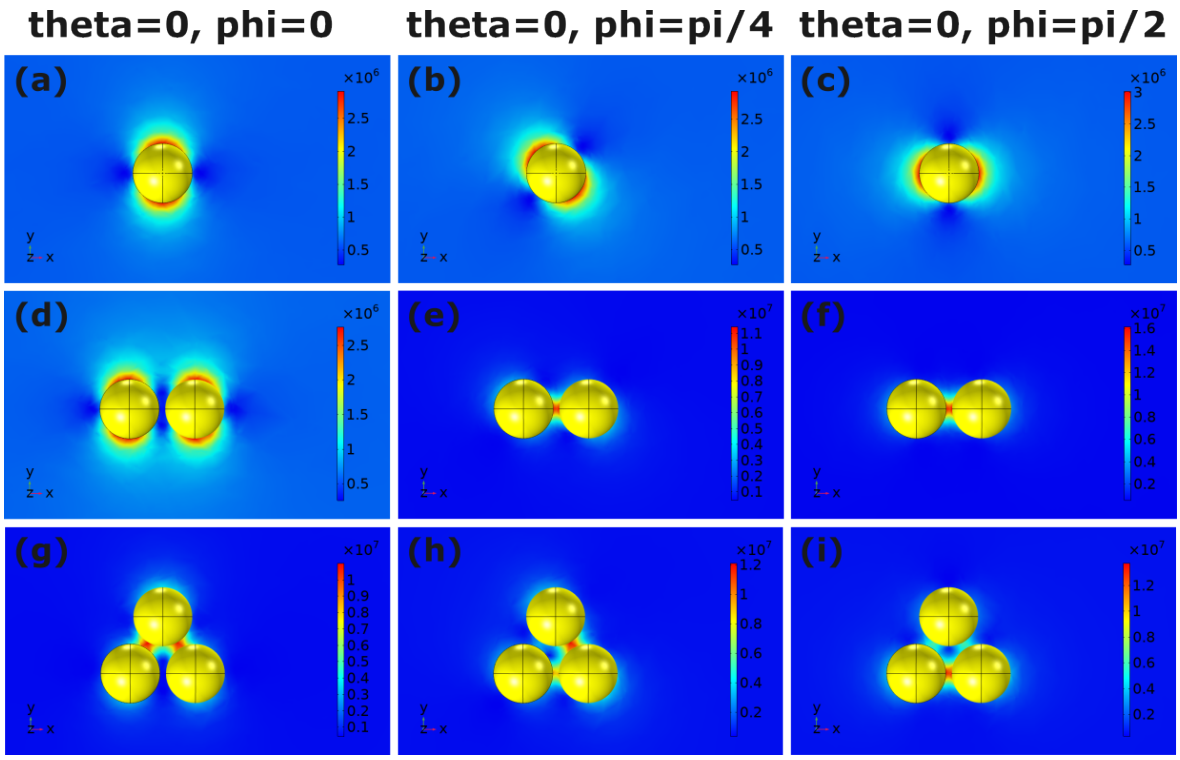

Figure 7.7: Local electric field distribution for AuNP arrangements at different polarization of the incident laser of wavelength 530 nm.

$\pi/2$ as depicted in the figure 7.7(e) and 7.7(f), respectively. Electric field amplitude is maximum for $\phi = \pi/2$ and minimum for $\phi = 0$ where no coupling can be found as shown in the figure 7.7(d). The electric field distributions for AuNP trimer for the three polarization have been shown in the figure 7.7(g-i).

Next, two AgNPs of diameter 50 nm separated by a distance 5 nm in air medium has been considered. Laser light from wavelength 350 nm to 800 nm have been allowed to incident on the nanoparticles. The scattered electic fields have been measured using the simulation software and plotted against incident wavelengths. In the figure 7.8(a), the peak of the electric field amplitude at 420 nm is the implication of maximum enhancemnt at this wavelength. Similarly, interaction of different wavelenghts of laser with two 50 nm AuNPs separated by a distance 5 nm have been calculated. Figure 7.8(b) represents a enhancement in the scattered electric field amplitude at 550 nm.

Next, simulation study have been performed to understand the effect of interparticle spacing with the localized electric field and the EF. Here, two AgNPs of diameter 50 nm interacting with a incident laser of wavelength 785 nm have been considered. Figure 7.9(a), 7.9(c) and 7.9(e) represent the local electric field amplitudes, and 7.9(b), 7.9(d) and 7.9(f) are the corresponding EF for interparticle spacings 2 nm, 3 nm and 4 nm, respectively. Figure 7.9 (g) depicts the variation of the local electric field and the EF with the interparticle distance from 2 nm to 10 nm for the same AgNPs of diameter 50 nm each. There is a decrease in the local electric field and the EF with the increase

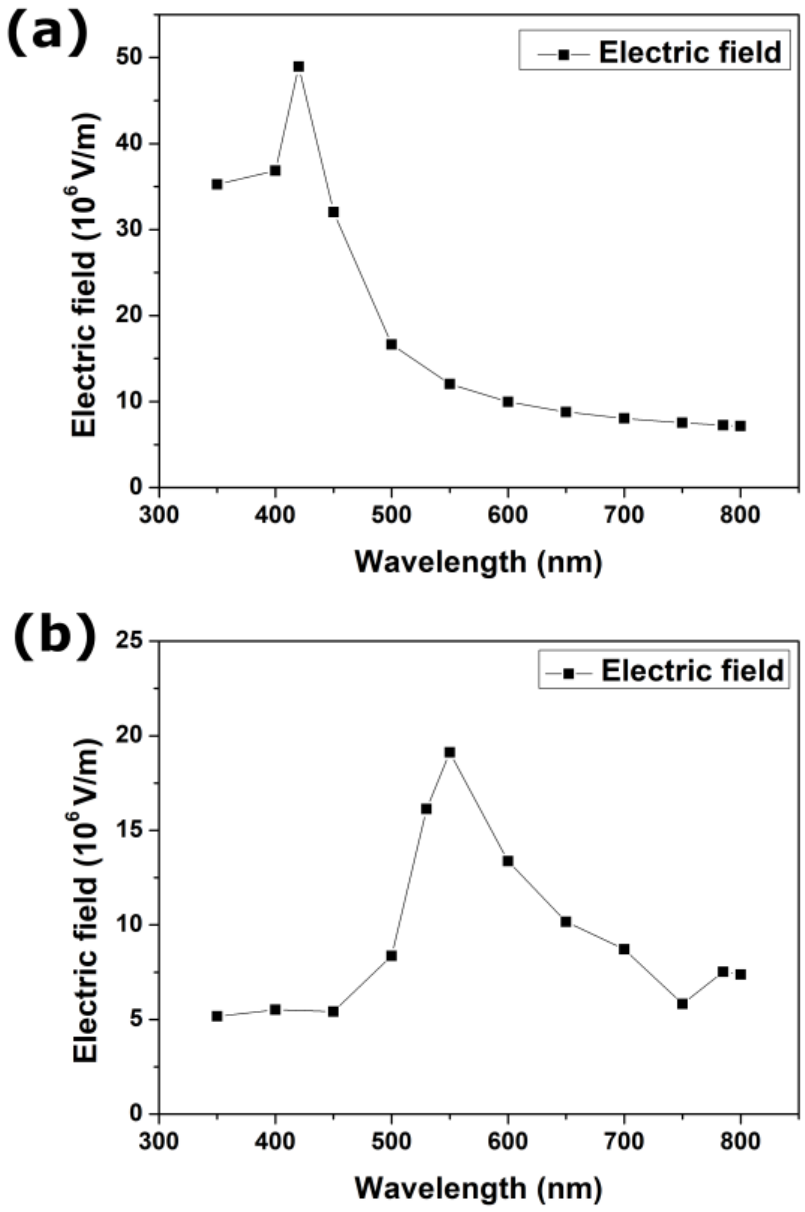

Figure 7.8: Maximum electric field variation at different incident laser wavelengths for (a) two AgNPs and (b) two AuNPs of diameter 50 nm each separated by a distance 5 nm.

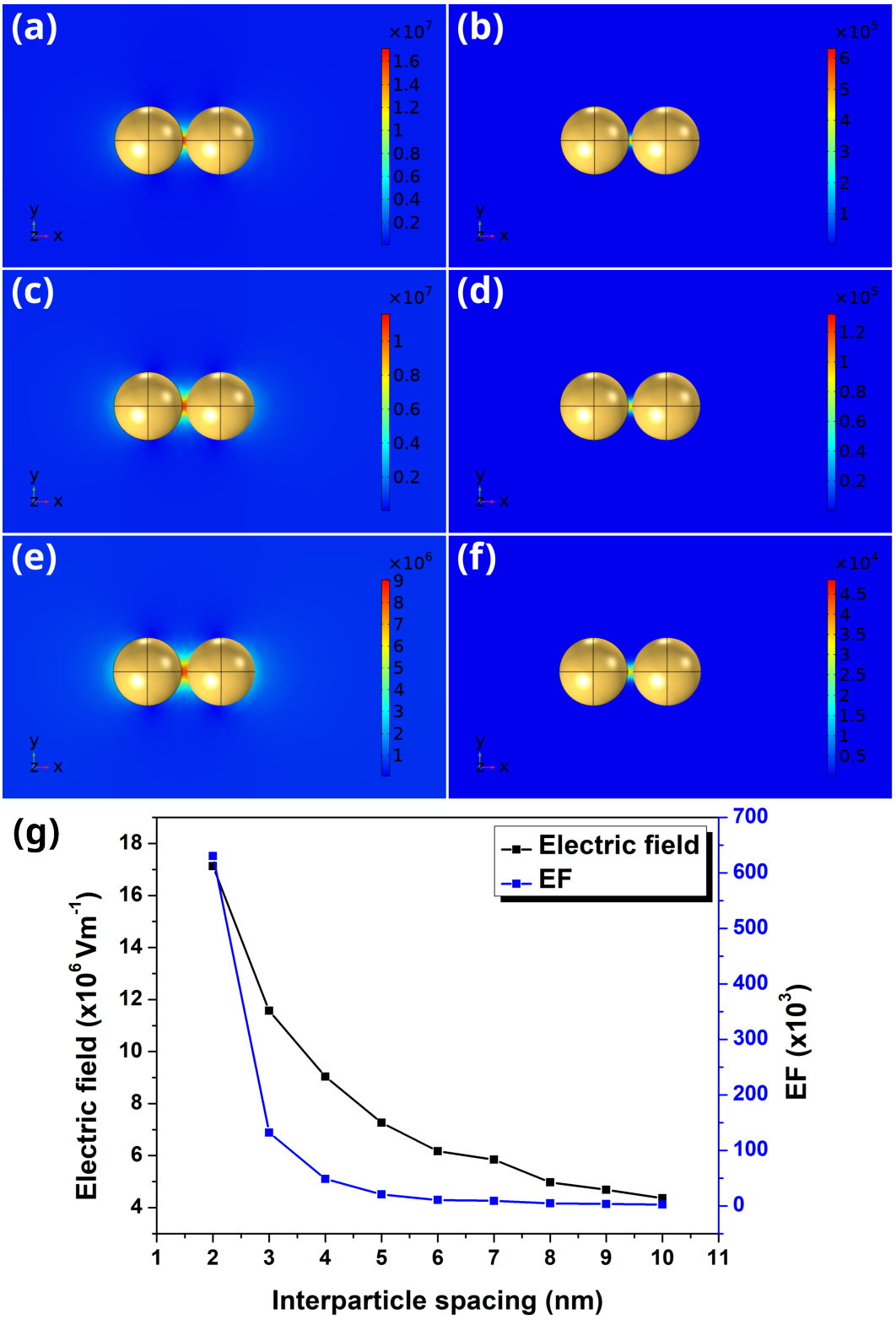

Figure 7.9: Simulation images of local electric field (a,c,e) and EF (b,d,f) for two AgNPs of diameter 50 nm each interacting with a laser of wavelength 785 nm. The interparticle spacing is varied, 2 nm (a,b), 3 nm (c,d) and 4 nm (e,f). (g) Local electric field and EF are plotted against the interparticle distance from 2 nm to 10 nm for the same AgNPs of diameter 50 nm each.

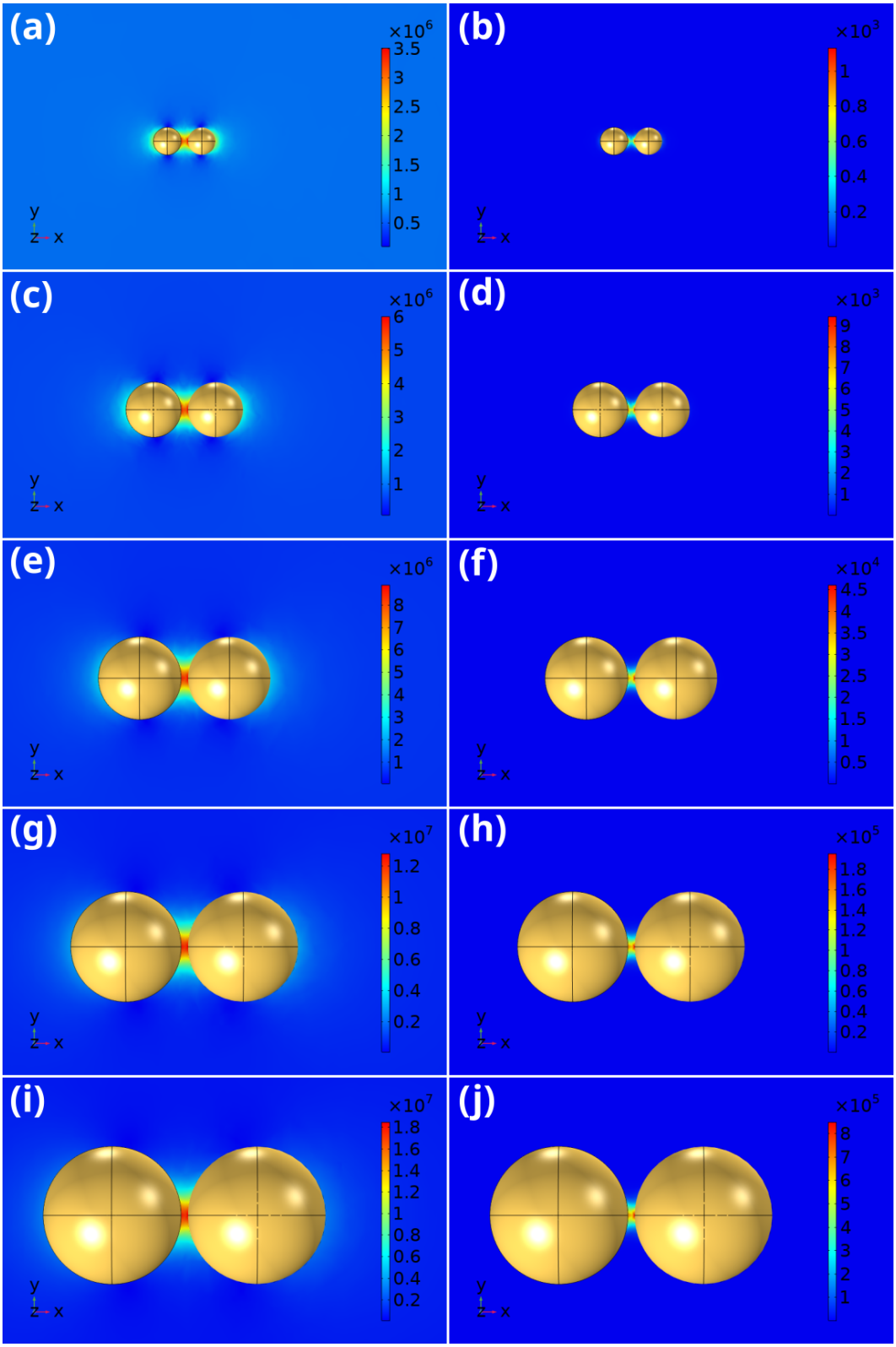

Figure 7.10: Simulation images of the local electric field (a,c,e,g,i) and the EF (b,d,f,h,j) for two AgNPs each of diameter 20 nm (a,b), 40 nm (c,d), 60 nm (e,f), 80 nm (g,h) and 100 nm (i,j), and separated by a distance 5 nm in air medium for a 785 nm incident laser.

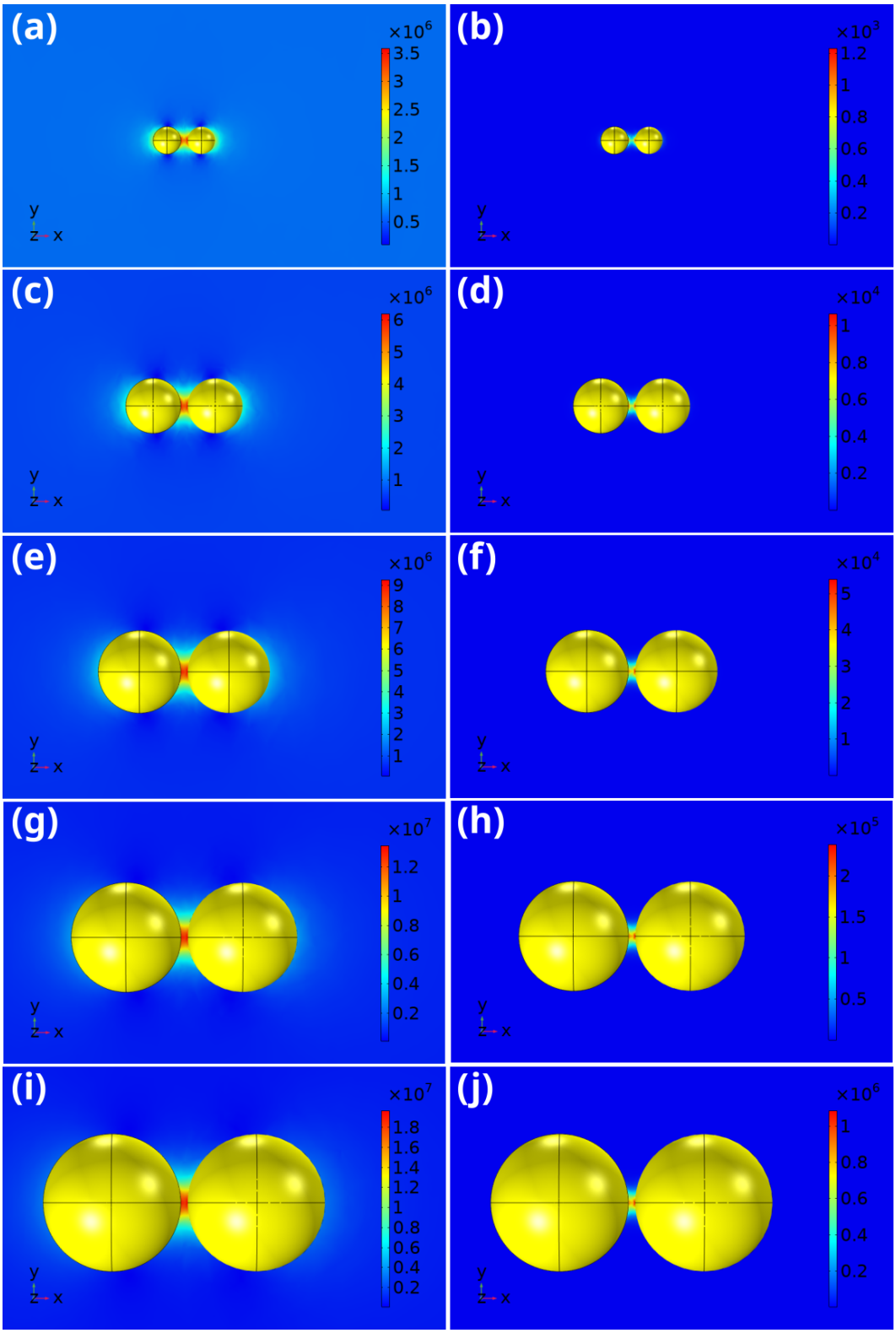

Figure 7.11: Simulation images of the local electric field (a,c,e,g,i) and the EF (b,d,f,h,j) for two AuNPs each of diameter 20 nm (a,b), 40 nm (c,d), 60 nm (e,f), 80 nm (g,h) and 100 nm (i,j), and separated by a distance 5 nm in air medium for a 785 nm incident laser.

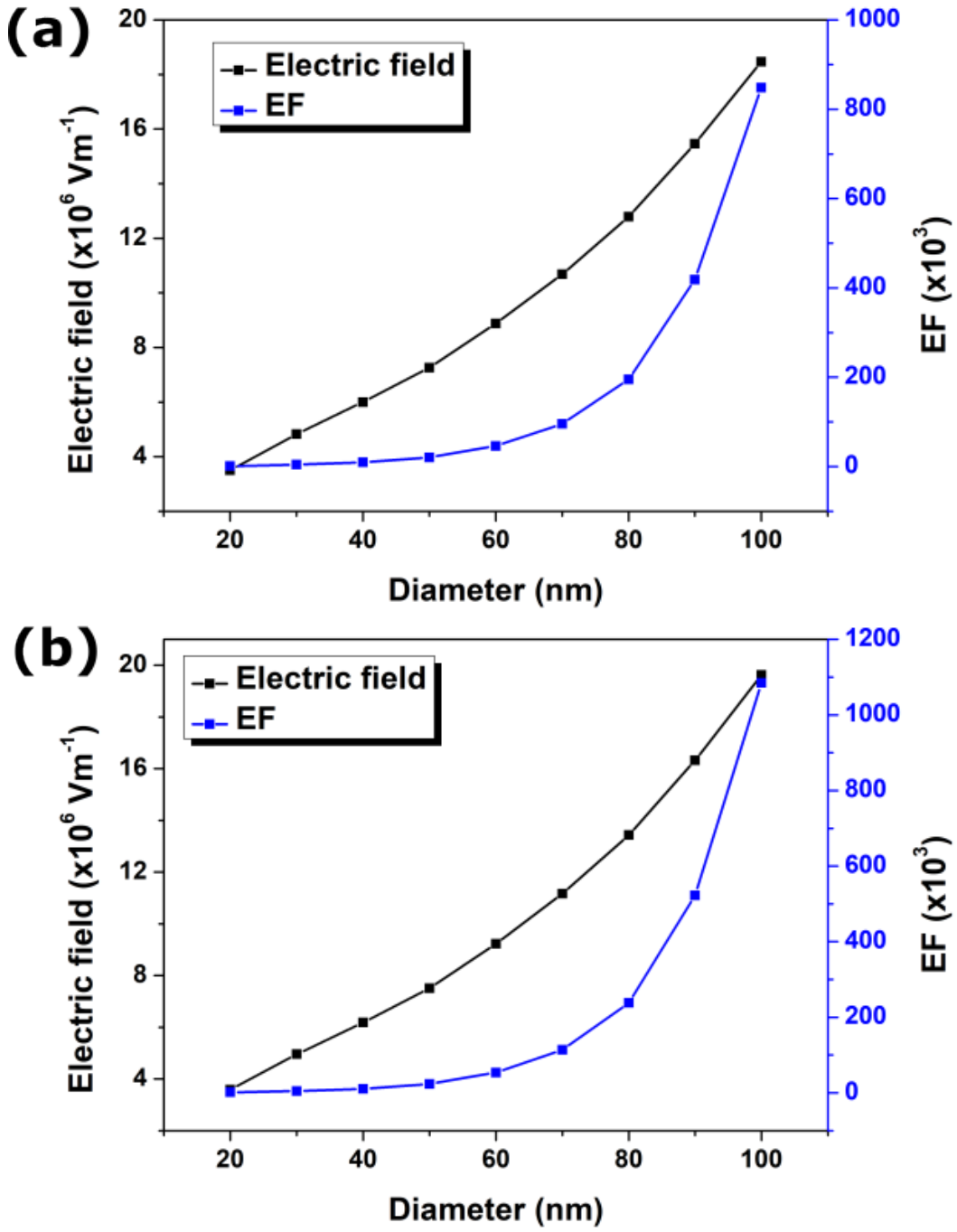

Figure 7.12: The local electric field and EF variation for two AgNPs (a) and two AuNPs (b) of diameter ranging from 20 nm to 100 nm, at a fixed 5 nm interparticle spacing and 785 nm incident laser.

in interparticle spacing.

Next, the variation of the local electric field amplitude and the EF with the diameter of the nanoparticles in AgNP and AuNP dimer have been studied. Here, the incident laser wavelength 785 nm and the interparticle spacing 5 nm have been kept fixed. First, size of the AgNPs are varied from 20 nm to 100 nm, and local electric field amplitude and the EF have been measured. For two AgNPs each of diameter 20 nm, 40 nm, 60 nm, 80 nm and 100 nm, the the local electric field amplitudes have been depicted in the figure 7.10(a), 7.10(c), 7.10(e), 7.10(g), 7.10(i), and the corresponding EF in the figure 7.10(b), 7.10(d), 7.10(f), 7.10(h), 7.10(j).

Same steps have been repeated for AuNP dimers of particle diameter 50 nm separated by a distance 5 nm and an incident light of wavelength 785 nm. The simulation images represent the local electric field in the figure 7.11(a), 7.11(c), 7.11(e), 7.11(g), 7.11(i), and the corresponding EF in the figure 7.11(b), 7.11(d), 7.11(f), 7.11(h), 7.11(j) for two AuNPs each of diameter 20 nm, 40 nm, 60 nm, 80 nm and 100 nm, respectively. Figure 7.12(a) and 7.12(b) represent the plot of local electric field and EF variation with the diamter of AgNP and AuNP dimer, respectively. It can be observed that with increase of the size to 100 nm the field amplitude and EF increases for both the nanoparticle systems at the particular wavelength.

Bibliography

[1] Saini, R. K., Sharma, A. K., Agarwal, A., and Prajesh, R. Near field fem simulations of plasmonic gold nanoparticle based sers substrate with experimental validation. *Materials Chemistry and Physics*, 287:126288, 2022.

[2] Multiphysics, C. Introduction to comsol multiphysics®. *COMSOL Multiphysics, Burlington, MA, accessed Feb*, 9(2018):32, 1998.

[3] Berenger, J.-P. A perfectly matched layer for the absorption of electromagnetic waves. *Journal of computational physics*, 114(2):185–200, 1994.

[4] Rakić, A. D., Djurišić, A. B., Elazar, J. M., and Majewski, M. L. Optical properties of metallic films for vertical-cavity optoelectronic devices. *Applied optics*, 37(22): 5271–5283, 1998.

List of publications

Research articles (Included in the thesis)

1. **Biswas, S.**, Devi, Y. D., Sarma, D., Hatiboruah, D., Chamuah, N., Namsa, N. D., & Nath, P. *Detection and analysis of rotavirus in clinical stool samples using silver nanoparticle functionalized paper as SERS substrate.* **Spectrochimica Acta Part A: Molecular and Biomolecular Spectroscopy**, 295, 122610, **2023**. https://doi.org/10.1016/j.saa.2023.122610

2. **Biswas, S.**, Devi, Y. D., Sarma, D., Namsa, N. D. & Nath, P. *Gold nanoparticle decorated blu-ray DVD as a highly reproducible SERS substrate for detection and analysis of rotavirus RNA in a laboratory environment.* **Journal of Biophotonics**, 15(11), e202200138, **2022**. https://doi.org/10.1002/jbio.202200138

Conferences and presentations

1. Bezbaruah, P., **Biswas, S.**, Chamuah, N., and Nath, P. *Extremely low-cost paper-based SERS substrate for detection and analysis of arsenic level in water.* National conference on light matter interaction at nanoscale 2019 (LMIN 2019). IGCAR, Tamil Nadu, India, **2019**.

2. **Biswas, S.**, Sarma, D., Chamuah, N., and Nath, P. *Simulation study of electric field enhancement and distribution during surface-enhanced Raman scattering experiment.* One day National Symposium on the occasion of National Science Day, Tezpur University, India, **2022**.

Other publications (Not included in the thesis)

1. Borah, J., Pathak, P., Bora, J., **Biswas, S.**, Nath, P., Pal, A. R., & Sarma, B. K. *High-yield conversion of lab waste to resources for the development of nanocomposite broadband photocatalysts embracing near-infrared plasmonic effects.* **Composites Part B: Engineering**, 111594, **2024**. https://doi.org/10.1016/j.compositesb.2024.111594

2. Sarma, D., Nath, K. K., **Biswas, S.**, Chetia, I., Badwaik, L. S., Ahmed, G. A. & Nath, P. *SERS determination and multivariate classification of antibiotics*

in chicken meat using gold nanoparticle–decorated electrospun PVA nanofibers. **Microchimica Acta**, 190(2), 1-11, **2023**.

https://doi.org/10.1007/s00604-023-05640-2

3. Sarma, D., **Biswas, S.**, Hatiboruah, D., Chamuah, N. & Nath, P. *100 GSM paper as an SERS substrate for trace detection of pharmaceutical drugs in an aqueous medium.* **Journal of Physics D: Applied Physics**, 55(38), 385102, **2022**. https://doi.org/10.1088/1361-6463/ac7b50

4. Hatiboruah, D., **Biswas, S.**, Sarma, D., & Nath, P. *A smartphone-based photometric and fluorescence sensing for accurate estimation of zinc ion in water.* **Sensors and Actuators A: Physical**, 341, 113586, **2022**. https://doi.org/10.1016/j.sna.2022.113586

5. Nath, M. P., **Biswas, S.**, Nath, P. & Choudhury, B. *Synergy of Adsorption and Plasmonic Photocatalysis in the Au–CeO2 Nanosystem: Experimental Validation and Plasmonic Modeling.* **Langmuir**, 38(24), 7628–7638, **2022**. https://doi.org/10.1021/acs.langmuir.2c01056

6. Rabha, D., **Biswas, S.**, Hatiboruah, D., Das, P., Rather, M., Mandal, M. & Nath, P. *An affordable, handheld multimodal microscopic system with onboard cell morphology and counting features on a mobile device.* **Analyst**, 2859-2869, **2022**. https://doi.org/10.1039/D1AN02317A

7. Das, P., **Biswas, S.**, Bhattacharya, S. S. & Nath, P. *Carbon Nanodot–Neutral Red-Based Photometric and Fluorescence Sensing for Trace Detection of Nitrite in Water and Soil Using Smartphone.* **ACS Applied Nano Materials**, 5(3), 3265-3274, **2022**. https://doi.org/10.1021/acsanm.1c03702

8. Kashyap, T., **Biswas, S.**, Ahmed, S., Kalita, D., Nath, P. & Choudhury, B. *Plasmon activation versus plasmon quenching on the overall photocatalytic performance of Ag/Au bimetal decorated g-C3N4 nanosheets under selective photoexcitation: A mechanistic understanding with experiment and theory.* **Applied Catalysis B: Environmental**, 298, 120614, **2021**. https://doi.org/10.1016/j.apcatb.2021.120614

9. Rabha, D., **Biswas, S.**, Chamuah, N., Mandal, M., & Nath, P. *Wide-field multimodal microscopic imaging using smartphone.* **Optics and Lasers in Engineering**, 137, 106343, **2021**. https://doi.org/10.1016/j.optlaseng.2020.106343